# Base flow decomposition for complex moving objects in linear hydrodynamics: Application to helix-shaped flagellated microswimmers

Ji Zhang [1,*] Mauro Chinappi [2,†] and Luca Biferale [3,‡]

[1]*Beijing Computational Science Research Center, Beijing 100193, China*
[2]*Department of Industrial Engineering, University of Rome, Tor Vergata, Via del Politecnico 1, 00133 Roma, Italy*
[3]*Department of Physics, INFN, University of Rome, Tor Vergata, Via della Ricerca Scientifica 1, 00133 Roma, Italy*

The motion of microswimmers in complex flows is ruled by the interplay between swimmer propulsion and the dynamics induced by the fluid velocity field. Here we study the motion of a chiral microswimmer whose propulsion is provided by the spinning of a helical tail with respect to its body in a simple shear flow. Thanks to an efficient computational strategy that allowed us to simulate thousands of different trajectories, we show that the tail shape dramatically affects the swimmer's motion. In the shear dominated regime, the swimmers carrying an elliptical helical tail show several different Jeffery-like (tumbling) trajectories depending on their initial configuration. As the propulsion torque increases, a progressive regularization of the motion is observed until, in the propulsion dominated regime, the swimmers converge to the same final trajectory independently on the initial configuration. Overall, our results show that elliptical helix swimmer presents a much richer variety of trajectories with respect to the usually studied circular helix tails.

## I. INTRODUCTION

Several micro-organisms move in liquids thanks to rotating flagella. For instance, the bacterium *Escherichia coli* has several flagella that form a rotating helical bundle [1], whereas other bacteria, such as *Pseudomonas aeruginosa*, exploit the same propulsion strategy but using a single helical flagellum [2,3]. The high swimming speed and the relatively simple geometry of such a kind of chiral microswimmer make them suitable for various applications and, in the past decade, artificial versions of flagellated microswimmers have been proposed for micromanipulation [4] and drug delivery [5].

The interaction between the helical flagellated microswimmers and the environment presents a rich behavior that has received extensive attention in the past decades [6,7]. Close to interfaces, helical flagellated microswimmers follow circular trajectories that are clockwise for solid walls [8–10] and counterclockwise for liquid-air interfaces [11–14]. Far from the wall, the hydrodynamic of active micro-organisms is highly affected by the local flow conditions. A relevant phenomenon is rheotaxis, i.e., the movement resulting from fluid velocity gradients. As shown by Fu *et al.* [15], the rheotaxis of flagellated microswimmers with helical tails is a purely physical phenomenon due to interplay between the velocity gradients and the shape of chiral flagella. Indeed, for a passive helix, the shear induces Jeffery-like tumbling motion parallel to the shear plane [16]. Along the orbit, elongated helices spend more time aligned with streamlines. Since this

configuration is not symmetric with respect to the shear plane, a chirality-dependent drift generally sets in. For an active helical microswimmer, the passive chirality-induced drift is often overwhelmed by the propulsion: The shear results in a preferential orientation of the swimmers along which, thanks to the self-propulsion, the swimmer moves [15,17]. Hence, the swimming direction is ruled by the shear, likely preventing the possibility of controlling the orientation of microswimmers in an assigned flow [15].

A way to escape from the monotonous rheotaxis in shear flow is to increase the number of degrees of freedom (DOF) of the microswimmers, for instance, employing multiple tails [18] or adaptively changing the angle between body and tail(s) [19]. The existence of external flexibility, however, complicates the control of microswimmers, particularly, in view of possible technological applications. Another possibility to escape from the rheotaxis is to break some symmetries of the swimmer geometry. In this aspect, interestingly, it has recently been shown that the change in the cross section of the ellipsoids from circle to ellipse can lead to chaotic orbits [20–22].

Inspired by this phenomenon, we numerically analyzed the dynamics of a microswimmer made by an axisymmetric body and by an elliptical helix, (i.e., a helix that lies on an elliptical cylinder) in a shear flow. The possible presence of a large variety of different trajectories, requires a systematic exploration of a large number of initial conditions. This, in turn, pushed us to develop and apply an accurate and fast computational approach based on a decomposition of dynamics in an active and a passive motion that allowed to speed up the simulations and to collect for each case thousands of trajectories. Our results show that the elliptical helix swimmer presents a much richer variety of possible trajectories with respect to the

*zhangji@csrc.ac.cn
†mauro.chinappi@uniroma2.it
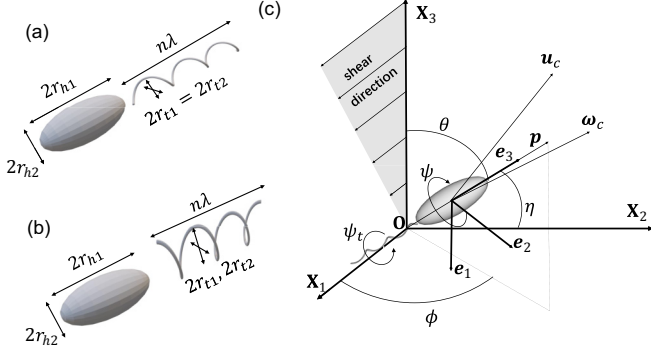‡Luca.Biferale@roma2.infn.it

FIG. 1. Sketch of microswimmer locomotion in a shear flow. The microswimmer body is a prolate ellipsoid of major axis $r_{h1}$ and minor axis $r_{h2}$. In (a) model I, the tail is a circular helix, i.e., a helix built on a circular cylinder of radius $r_{t1}$, whereas in (b) model II, the tail is an elliptical helix, i.e., a helix built on an elliptical cylinder of radii $r_{t1}$ and $r_{t2} = 3r_{t1}$. (c) The shear flow is on the $\mathbf{X}_1\mathbf{X}_3$ plane of the global coordinate frame $\mathbf{OX}_1\mathbf{X}_2\mathbf{X}_3$. A body coordinate frame $\mathbf{O}'\mathbf{e}_1\mathbf{e}_2\mathbf{e}_3$ moves with the swimmer body. The polar $\theta$ azimuthal $\phi$ and rotation $\psi$ angles are used to describe the orientation of the body frame with respect to the global frame. Moreover, we also define the angle between the swimmer axis $\boldsymbol{p} = \mathbf{e}_3$ and $\mathbf{X}_2$ as $\eta = \arccos(\sin\theta \sin\phi)$. The tail rotates with respect to the $\mathbf{e}_3$ so that each point of the rigid tail describes a circle on plane $\mathbf{e}_2\mathbf{e}_3$ with $\psi_t$ as the corresponding rotation angle. The motion of the microswimmer body is completely defined when the translational velocity $\boldsymbol{U}$ of the body center, the body rotational velocity $\boldsymbol{\Omega}$, and the tail spinning $\omega_t = \dot{\psi}_t$ are given.

well studied circular helix tails. In particular, we found for an elliptical helical tail a much higher spinning frequency is needed to control the asymptotic swimming regime.

## II. SETUP AND METHOD

Two kinds of microswimmers are compared in this paper: One with a circular helical tail, i.e., a helix that lies on a circular cylinder (model I) and one with an elliptical helical tail, i.e., a helix that lies on a cylinder of the elliptical section (model II), see Fig. 1. For both models, the body is a prolate ellipsoid of radii $r_{h1}$ and $r_{h2}$, and the center of the body is indicated as $\boldsymbol{x}_c$. A body coordinate frame $\mathbf{O}'\mathbf{e}_1\mathbf{e}_2\mathbf{e}_3$ with the origin at $\boldsymbol{x}_c$ and $\mathbf{e}_3$ oriented as the major ellipsoid axis is defined. Concerning the tail, its centerline follows the helix equation in the body coordinate frame,

$$\boldsymbol{r} = (r_{t1}\cos(2\pi s), r_{t2}\sin(2\pi s), \lambda s - \delta_{bt}), \quad (1)$$

where $s \in [-n/2, n/2]$ with $n$ as the number of periods of the tail, $\delta_{bt}$ is the distance from $\boldsymbol{x}_c$ to the tail center, $\lambda$ is the pitch of the helix, and $r_{t1}$ and $r_{t2}$ are the radii of the elliptical cylinder on which the helix lies. For the circular helix, $r_{t1} = r_{t2}$, whereas for elliptical helix $r_{t1} = 3r_{t2}$. The flagellum section is a cylinder of radius $\rho_t$. All the details of the swimmer geometry are reported in Appendix.

The microswimmer has seven DOFs: three translation DOFs $\boldsymbol{x}_c = (x_{c1}, x_{c2}, x_{c3})$, three rotational DOFs $\boldsymbol{\theta}_c = (\theta, \phi, \psi)$ plus the tail orientation $\phi_t$ with respect to the body. The body orientation is defined by the unit vector $\boldsymbol{p} = (\sin\theta \cos\phi, \sin\theta \sin\phi, \cos\theta)$ here expressed as a func-

tion of the polar $\theta$ and the azimuthal $\phi$ angles. It is also instrumental to define angle $\eta = \arccos(\sin\theta \sin\phi)$ between $\boldsymbol{p}$ and $\mathbf{X}_2$, see Fig. 1. The value $\eta = 0$ ($\eta = \pi$) corresponds to a configuration where the microswimmer is perpendicular to the shear plane and points toward positive (negative) $\mathbf{X}_2$, whereas $\eta = 0.5\pi$ corresponds to the microswimmer lying on the shear plane. The swimmer body moves with translational velocity $\boldsymbol{U}$ and rotational velocity $\boldsymbol{\Omega}$ whereas the tail spins at a constant speed and, consequently, $\omega_t = \dot{\psi}_t$.

The governing equations of fluid velocity $\boldsymbol{u}$ and pressure $p$ fields are the Stokes equations,

$$\nabla \cdot \boldsymbol{u} = 0, \quad (2)$$

$$\mu\nabla^2\boldsymbol{u} = \nabla p, \quad (3)$$

with $\mu$ as the fluid viscosity. The no-slip boundary condition is applied on the surfaces of the head,

$$\boldsymbol{u}(\boldsymbol{x}) = \boldsymbol{U} + \boldsymbol{\Omega} \times \boldsymbol{r}, \quad (4)$$

and of the tail of the microswimmer,

$$\boldsymbol{u}(\boldsymbol{x}) = \boldsymbol{U} + (\boldsymbol{\Omega} + \omega_t\boldsymbol{p}) \times \boldsymbol{r}, \quad (5)$$

where in both equations $\boldsymbol{r}$ indicates the relative position of the boundary point with respect to the center of the swimmer head $\boldsymbol{x}_c$. Note that, in general, $\boldsymbol{U}$ and $\boldsymbol{\Omega}$ are not parallel to the swimmer orientation $\boldsymbol{p}$. Thus, there exists no simple relation between the active spin $\omega_t$ and the velocities $(\boldsymbol{U}, \boldsymbol{\Omega})$.

The method for the solution of the swimming problem is briefly sketched in the following whereas details are reported in Appendix. The fundamental step is to get the swimmer generalized velocity $(\boldsymbol{U}, \boldsymbol{\Omega})$ as a function of the swimmer configuration and tail spinning velocity $\omega_t$. Once $(\boldsymbol{U}, \boldsymbol{\Omega})$ are known, the standard rigid body kinematic equations can be solved for the swimmer head. The swimming problem is solved by decoupling the $(\boldsymbol{U}, \boldsymbol{\Omega})$ into two parts where the active part $(\boldsymbol{U}_a, \boldsymbol{\Omega}_a)$ corresponds to the movement of the microswimmer in a bulk fluid at rest whereas the passive part $(\boldsymbol{U}_p, \boldsymbol{\Omega}_p)$ corresponds to a passive swimmer ($\omega_t = 0$) immersed in the external flow field $\boldsymbol{u}_b$. Thanks to the linearity, the active part can be expressed as $\boldsymbol{U}_a = \omega_t\boldsymbol{R}\tilde{\boldsymbol{U}}_a$, $\boldsymbol{\Omega}_a = \omega_t\boldsymbol{R}\tilde{\boldsymbol{\Omega}}_a$ where $\boldsymbol{R}$ is the rotation matrix that transforms the expression of a vector in the body reference frame into its expression in the global reference frame and $(\tilde{\boldsymbol{U}}_a, \tilde{\boldsymbol{\Omega}}_a)$ are the velocities for a microswimmer swimming with $\omega_t = 1$ in a configuration where body and global frames coincide. Concerning the passive part, instead, we exploit the local decomposition of $\boldsymbol{u}_b$ in three components, a rigid translation at $\boldsymbol{x}_c$, a rigid rotation $\boldsymbol{\omega}_p^S$ (associated with the antisymmetric part of the velocity gradient $S_{ij}$) and a deviatoric part (symmetric part of the velocity gradient $E_{ij}$). The deviatoric part $E_{ij}$ can be further decomposed into five components. For each of them, we can solve a swimming problem and get the contributions to the swimmer translational $\boldsymbol{U}$ and angular $\boldsymbol{\Omega}$ velocities. Combining all those contributions, the microswimmer velocity in an external flow is obtained as

$$\boldsymbol{U} = \omega_t\boldsymbol{R}\tilde{\boldsymbol{U}}_a + \boldsymbol{U}_p^b + \boldsymbol{R}\sum_{k=1}^{5}\tilde{\beta}_k\tilde{\boldsymbol{U}}_k^E, \quad (6)$$
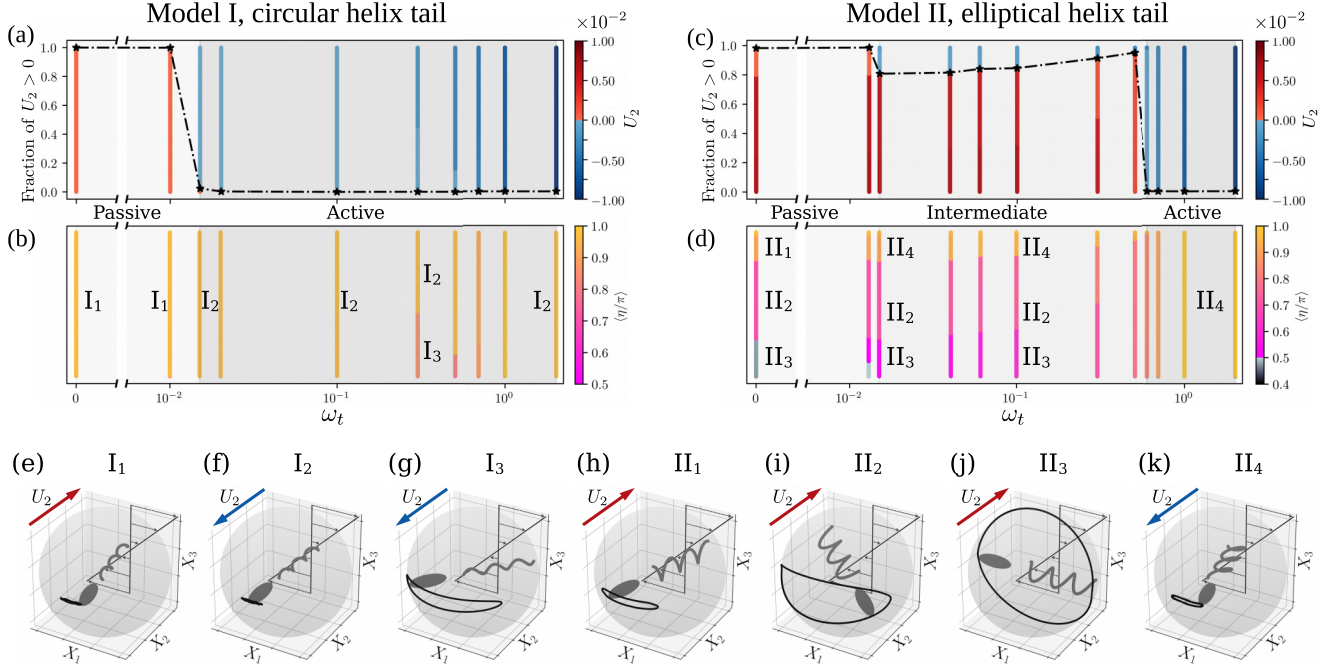
FIG. 2. Microswimmer motion in a simple shear flow. For each case, from $10^3$ to $10^4$ simulations with different initial conditions were run. Panel (a) reports the fraction of the circular helix swimmers that have a drift velocity oriented as $\mathbf{X}_2$ ($U_2 > 0$). The bars in panel (a) indicate the lateral velocity $U_2$ for the different initial conditions whereas the bars in panel (b) refer to the normalized average angle $\langle \eta/\pi \rangle$ between $\mathbf{X}_2$ and the microswimmer head orientation $\boldsymbol{p}$. In the passive regime, all the trajectories converge to the same final state [$\mathrm{I}_1$, panel (e)] where the swimmer is oriented as $-\mathbf{X}_2$ whereas its velocity is $U_2 \cong 10^{-4}$. In the active regime, the swimmer is again oriented as $-\mathbf{X}_2$, but $U_2 < 0$, see configuration (f) $\mathrm{I}_2$ and (g) $\mathrm{I}_3$. The dot-dashed line corresponds to the fraction of swimmers for which $U_2 > 0$. Panels (c) and (d) refer to velocity $U_2$ and orientation $\langle \eta/\pi \rangle$ for the elliptical helix tail. Here, a new intermediate regime appears between the active and passive regimes. In this intermediate regime, both positive and negative drift velocities $U_2$ are possible. Panels (e)–(k) report examples of the swimmer Jeffery-like tumbling motion (shear on the $X1X3$ plane). The solid lines on the spheres represent the direction of the swimmer axis $\boldsymbol{p}$ along one period whereas the red and blue arrows refer to the direction of the average velocity along $X_2$.

$$\boldsymbol{\Omega} = \omega_t \boldsymbol{R} \tilde{\boldsymbol{\Omega}}_a + \boldsymbol{\Omega}_p^S + \boldsymbol{R} \sum_{k=1}^{5} \tilde{\beta}_k \tilde{\boldsymbol{\Omega}}_k^E, \qquad (7)$$

where the first term on the right hand side is the active contribution, the second term is the uniform translation $\boldsymbol{U}_p^b$ and rotation $\boldsymbol{\Omega}_p^S$ due to the external flow, and the last terms are the five contributions due to the deviatoric part of the velocity gradient. The weights $\tilde{\beta}_k$ depend only on $\boldsymbol{u}_b$ and on the swimmer orientations, details are reported in Appendix. It is worth noting that, as a first approximation, a more appropriate model for the head-tail coupling is to fix the exchanged torque [23,24]. However, in our case, the head-tail coupling enters only in the active part of Eqs. (6) and (7). Since the active part corresponds to the movement of the microswimmer in a bulk fluid at rest, the tail spin $\omega_t$ is proportional to the motor torque and, hence, considering a fixed spin or a fixed torque only amounts to a linear rescaling with no effect on the observed phenomenology.

The main advantage of the proposed method is that only six solutions of the swimming problem are needed; one for $(\tilde{\boldsymbol{U}}_a, \tilde{\boldsymbol{\Omega}}_a)$ and five for $(\tilde{\boldsymbol{u}}_k^E, \tilde{\boldsymbol{\Omega}}_k^E)$. These swimming problems can be solved with any Stokes solver. Here we use the method of fundamental solution (MFS) [25] that is summarized in Appendix. Once these solutions are known, one can integrate the

rigid body kinematics to get the swimmer trajectory. Here, this integration step is performed using a quaternion formulation and a fourth order Runge-Kutta method.

## III. RESULTS

In this paper, the microswimmer is immersed in an unbounded shear flow,

$$\boldsymbol{u}_b = (x_3 \tau_s, 0, 0), \qquad (8)$$

Without loss of generality, we select as the time unit $1/\tau_s$ and as the length unit of length $r_{h1}$ the larger axis of the ellipse. Due to the linearity of the problem, spin $\omega_t$ is the only crucial parameter for a given microswimmer. For both the circular (model I) and the elliptical (model II) helical tail microswimmers, we studied the motions at different tail spinning velocities $\omega_t$. For each $\omega_t$, we simulated from $10^3$ to $10^4$ trajectories starting from different initial conditions with random orientation. The center of the head is initially placed in the origin at $t = 0$. In all the cases, after a transient, the swimmer orientation converges to periodic trajectories. Concerning the swimmer translation, different scenarios are possible depending on the swimmer tail geometry, its spinning velocity $\omega_t$, and its initial condition. A summary of the different possibilities is reported in Fig. 2 and discussed in the following sections.

### A. Circular helix

For the circular helix swimmer, in the passive case (tail spinning velocity $\omega_t = 0$) after a transient, the swimmer is always oriented along $-\mathbf{X}_2$, i.e., normally to the shear plane $\mathbf{X}_1\mathbf{X}_3$, and it moves along $\mathbf{X}_2$, i.e., $U_2 > 0$. In Fig. 2(a), those information are condensed in panel (a) where the fraction of the trajectories that result in final drift $U_2 > 0$ can be read on the left axes whereas the colored bars indicate the actual value of $U_2$. For instance, the orange bar at $\omega_t = 0$ means that all the $10^3$ initial conditions result in a slightly positive terminal velocity $U_2 \cong 1.01 \times 10^{-4}$ whereas the blue bar at $\omega_t = 0.015$ indicates that almost all the swimmers reach a final velocity of $U_2 \cong -3.00 \times 10^{-6}$. Figure 2(b), instead, reports the orientation $\eta$ averaged on a period. For the pure passive case $\omega_t = 0$, we always get $\langle \eta \rangle \cong \pi$, i.e., the swimmer is oriented perpendicularly to the shear plane. This passive swimmer regime is indicated as $I_1$ and a sketch of its periodic orbits is reported in Fig. 2(e) and in the Supplemental Material Video SM1 [26]. This result is in agreement with the shear-induced separation of pure circular helix discussed in Ref. [15] where it was shown that microswimmers point perpendicularly to the shear plane in the direction here indicated as $-X_2$. A similar behavior is also observed for low spinning velocity $\omega_t < 0.015$.

A further increase in the tail spinning results in a first change in the dynamics. The average orientation of the swimmer is the same $\langle \eta \rangle \cong \pi$, but now the drift velocity is positive $U_2 > 0$, $I_2$ Fig. 2(f). This is expected, indeed, as $\omega_t$ increases, the swimmer propulsion becomes more relevant until, finally, it dominates over the passive drift induced by the shear. Interestingly, in some intervals of the spinning speed, an additional kinematics appears, $I_3$ Fig. 2(g). The swimmer undergoes a Jeffery-like motion with $\langle \eta \rangle \in [0.8, 0.9]\pi$. This motion is characterized by a slightly smaller value of the average velocity $U_2$. Depending on the initial condition, some trajectories converge to a motion of the $I_2$ kind and others to $I_3$. Overall, those data indicate that the shear always orients the swimmer along $-\mathbf{X}_2$. For small tail spinning (passive case) the shear dominates the dynamics and the swimmer moves in the $\mathbf{X}_2$ direction whereas, for large tail spinning (active case), the self-propulsion dominates, and the swimmer moves in the $-\mathbf{X}_2$ direction.

### B. Elliptical helix

A much richer scenario occurs for swimmers with an elliptical helix tail, model II, Fig. 2(c). In the passive case, we observed three main different periodic trajectories. The overall drift is positive $U_2 > 0$ in this region as for model I. The average orientation $\langle \eta/\pi \rangle$, however, is significantly different. The first kind of trajectory $II_1$ orientates along $-\mathbf{X}_2$ as for model I. The other two kinds of trajectories, $II_2$ and $II_3$, present Jeffery-like tumbling behaviors that differ from $II_1$, see Figs. 2(h)–2(j) and Videos SM2–SM4 of the Supplemental Material [26]. In particular, for $II_3$ we observe that the tumbling occurs almost on the shear plane. Similar to the shear-induced separation of pure helix [16], such a kind of tumbling (Jeffery-like) motion on the shear plane is associated with a lateral velocity ($U_2$) of the microswimmer that, in our case, is larger than the one corresponding to $II_1$, see Fig. 2(c).
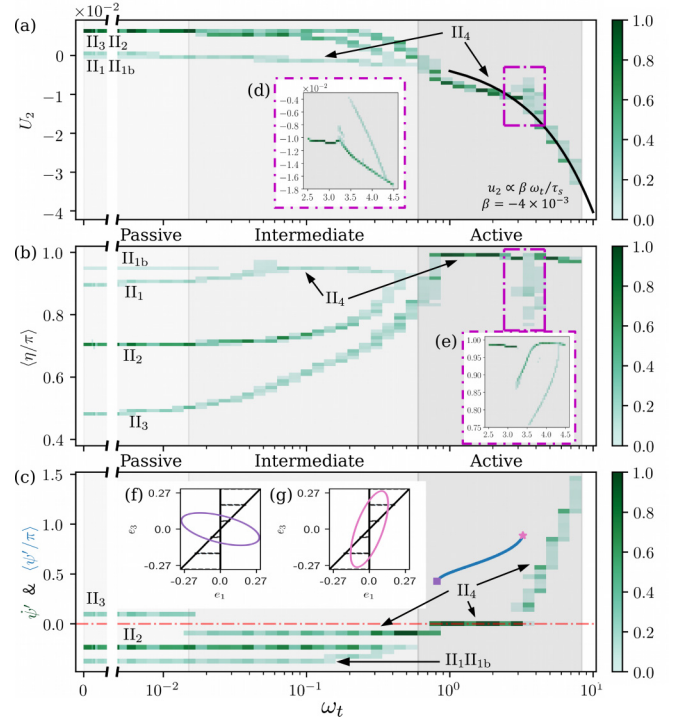


FIG. 3. Elliptical helix tail microswimmer. (a) Lateral velocity $U_2$, (b) normalized average angle $\langle \eta/\pi \rangle$, and (c) the absolute tail spin $\dot{\psi}' = \dot{\psi} + \dot{\psi}_t$ as functions of $\omega_t$. Results refer to 450 trajectories for each $\omega_t$. The green color scale indicates the probability that one initial condition converges to the corresponding value on the vertical axis, for instance, in the passive case, almost 75% of the swimmers converge to the trajectory $II_2$ that corresponds to $\langle \eta \rangle \cong 0.7\pi$ (dark green). The black solid line in panel (a) is the velocity of the same microswimmer in a fluid at rest. Panels (d) and (e) report a detailed view of the regions enclosed by the violet dotted boxes. The *freezing tail* phenomenon discussed in the text is sketched in panels (f) and (g) whereas the corresponding average $\psi'$ is reported as a solid blue line between $0.8 < \omega_t < 3.2$ in panel (c).

No simple rules are found to associate the final microswimmer trajectory to its initial orientation, see the Supplemental Material Sec. S1 [26] where examples of the time evolution of the orientation $\mathbf{p}$ are reported together with a diagram representing the domains in the orientation space that led to $II_1$–$II_3$ trajectories.

As spinning speed $\omega_t$ increases, the system undergoes a gradual regularization. We still observe three different kinds of trajectory, but the values of the average orientation $\langle \eta/\pi \rangle$ of $II_1$–$II_3$ get closer, until they merge. In this intermediate regime, trajectory $II_1$ switches from positive to negative $U_2$ and, for this reason, we renamed it as $II_4$, Fig. 2(l). Further increases in $\omega_t$ brings the system to a fully active regime where only the $II_4$ trajectory is observed: The swimmer is oriented along $-\mathbf{X}_2$ with $U_2 < 0$. This regime is analogous to the active regime for the circular helical tail, the $I_2$ trajectory.

To better characterize the elliptical helical tail microswimmer, we performed additional simulations that allowed us to observe further details of the swimmer motion. Results are reported in Fig. 3(a) for the lateral velocity $U_2$ and in Fig. 3(b) for the normalized average angle $\langle \eta/\pi \rangle$. For each $\omega_t$

we performed 450 simulations with random initial orientation. The green color scale corresponds to the probability that the swimmers reach a steady state with the corresponding value of $U_2$ and $\langle \eta/\pi \rangle$. For instance, at low $\omega_t$ (passive regime), four kinds of stable trajectories exist. Three of them, $II_1$–$II_3$, were already discussed in Fig. 2. The last one, indicated as $II_{1b}$, corresponding to $\langle \eta \rangle \sim 0.95\pi$, is quite rare [light green in Fig. 3(b)] and very similar to $II_1$. As already discussed in Fig. 2, the trajectories oriented perpendicularly to the shear plane ($II_1$ and $II_{1b}$ for which $\langle \eta \rangle \in [0.9, 1]\pi$) have almost no lateral motion ($U_2 \cong 0$). In contrast, the other two kinds of trajectories, characterized by Jeffery-like tumbling close to the shear plane ($II_2$ and $II_3$), show a significant lateral motion, $U_2 > 0$, see also Figs. 2(i) and 2(j). Moreover, Fig. 3 also better evidences how, through increasing in tail spin $\omega_t$, the tumbling trajectories $II_2$ and $II_3$ progressively converge towards the $-X_2$ axes as apparent from the increase in $\langle \eta/\pi \rangle$. Finally, in the active regime, all the trajectories merge into a single kind where the swimmer is oriented normal to the shear plane $\langle \eta \rangle \cong \pi$.

### C. Freezing spin

Nevertheless, some islands of complexity persist in this active region. For instance, the microswimmer is *frozen* by the shear flow for spinning $0.8 < \omega_t < 3.2$. The tail of the microswimmer, when seen from the global reference frame, does not spin along the swimmer axis $\boldsymbol{p}$. This is apparent in Fig. 3(c) where the time derivative of angle $\psi'$ is reported. In essence, the tail rotates with respect to the head ($\dot{\psi}_t = \omega_t$ is imposed in our model) but the rotation of the head with respect to the global reference frame exactly counter balances the spinning ($\psi' = \psi + \psi_t$, $\dot{\psi}' = \dot{\psi} + \dot{\psi}_t$, hence, $\dot{\psi}' = 0 \Rightarrow \dot{\psi} = -\dot{\psi}_t$), see the Supplemental Material video SM5 [26]. This is a peculiar behavior that occurs only for the elliptical helical tail and not for the circular one and it represents a further indication that slight changes in the swimmer geometry may lead to new phenomena. In fact, the tail of the microswimmer experiences a propulsion torque due to propulsion as well as a shear torque due to local velocity gradient. The balance between the two torques on the tail leads to the *freezing*. For the lowest spinning velocity for which the *freezing* occurs, i.e., $\omega_t = 0.81$, the propulsion torque is small. Thus, the mayor axis of the tail section is almost parallel to the shear velocity direction and, consequently, the torque induced by the shear on the tail is small as in Fig. 3(f). As the tail spinning $\omega_t$ increases, the propulsion torque increases, and the new balance is found for larger values of $\psi'$. The maximum shear torque is achieved when the mayor axis of the tail section is vertical and, indeed, the last value of $\omega_t = 3.24$ for which this tail's freezing occurs corresponds to $\psi' \approx \pi$, see Fig. 3(g).

Another unexpected behavior occurs for $\omega_t \in (3, 4.5)$ where we observe that, again, the swimmer may converge towards multiple different trajectories, see Figs. 3(d) and 3(e). All these trajectories have a negative $U_2$ and their oscillation around the $X_2$ axis is limited $\langle \eta/\pi \rangle > 0.7$. For these reasons they can be overall classified as $II_4$. Only after this last region of complexity, the motion gets finally regularized. In this fully active regime, the final swimmer speed is linear in the tail

spinning $U_2 = \beta\omega_t$ with $\beta = -4.02 \times 10^{-3}$. This is expected, indeed, when the tail spin is large, the final swimmer speed is dominated by the propulsion. Indeed, the value of $\beta$ we observed is the same as we got in a simulation of the active swimmer moving in a fluid at rest represented as a black solid line in Fig. 3(a). In essence, in the active regime, the shear selects the swimmer orientation, and the final speed is controlled by the tail spin. In the active regime, the swimmer dynamics is predictable and controllable: Any initial condition results in the same final trajectory.

## IV. CONCLUSION

In this paper, we proposed an efficient computational method for the analysis of microswimmer motion in external flows. We applied our method for the analysis of microswimmers whose propulsion is due to the spinning of a flagellum (*E.coli*-like swimmers). Once the swimmer geometry is selected, the entire range of spinning speed of the tail can be explored by solving only six swimming problems. This allowed us to simulate thousands of different trajectories. We compared the motions of two different swimmers, one carrying a circular helical tail, i.e., a helix that lies on a circular cylinder, that is, the typical geometry studied in previous theoretical and computational works, and another one carrying an elliptical helical tail. The alteration of the tail shape from circular helix to elliptical helix gives rise to a much richer scenario where different tumbling (Jeffery-like) trajectories can be observed under the same external flow condition and for the same tail spinning speed. As the propulsion torque increases, a progressive regularization of the motion is observed until, in the propulsion dominated regime, the swimmers converge to the same final trajectory for all the initial configurations. These results may have some implications on the biology of micro-organisms that exploit this propulsion mechanism. Indeed, the complex Jeffery-like tumbling we observed in the shear dominated regime may provide an alternative way to increase the capability of a microswimmer to explore the space that may cooperate with the well known *run and tumble* motion [27]. On the other hand, the high sensitivity to the shape of the tail implies that the micro-organism must reach a larger spinning frequency in order to have a full control of its asymptotic swimming direction. As a result, the presence of more than one steady state also has to be carefully taken into account when designing artificial microswimmers whose motion in external flows needs to be controlled.

## APPENDIX: DETAILS ON THE METHODS

In this Appendix, we discuss the approach we employed for the solution of the swimming problem for an active microswimmer with a single intrinsic DOF swimming in an external flow. The DOF is the spin of the tail with respect to

the microswimmer body. This model can be easily extended to multiple DOFs. Our method is a combination of known approaches for the solution of the Stokes equation that, for completeness, are reported in the following sections. The crucial idea is to decompose the rate of strain in five base components. This allows to reduce the solution of the swimming problem to six solutions of the Stokes equation, one for the active propulsion and five for the passive one. These swimming problems can be solved with any Stokes solver. Here we employed the MFS [25] Before entering in the details of our formulation, we briefly mention some alternative approaches for the swimming problem.

Modeling the motion of a microswimmer using multiple rigid bodies is a relatively common approach (see, e.g., Refs. [10,12]). A key to calculate the trajectory of a microswimmer is to compute the generalized velocity $(\boldsymbol{U}, \boldsymbol{\Omega})$, that can be calculated solving the Stokes equations plus the force- and torque-free conditions [7]. The boundary element method is commonly used for Stokes equations [10,28], although the solving method can be replaced by other formulations, such as the method of regularized Stokeslets [29–31], the boundary integral method [32], and the spectral boundary element method [33]. Since usually it is computationally expensive to calculate the generalized velocity $(\boldsymbol{U}, \boldsymbol{\Omega})$ directly using full solution of the Stokes equation, several approximate theories were developed for rigid body motion in Stokes flows. Following the work of Fu *et al.* and Marcos *et al.* [15,16], Mathijssen *et al.* [34] developed an approximate formulation of an ideal chiral object using the resistive force theory that allowed to study bacteria rheotaxis close to a surface. Another alternative approach is to calculate the generalized mobility matrix of the system [35]. For a three sphere swimmer model [36], a quadrupole order accurate multipole expansion was recently employed to study the swimmer kinematics close to a wall under a shear flow [37]. The possibility to extend this promising approach to more complex swimmer geometries is, however, an open issue.

### 1. Fundamental solution of the Stokes equation

Here, we briefly summarize the MFS [25]. In the creeping flow limit, the governing equation for the fluid velocity $\boldsymbol{u}$ and pressure $p$ due to a point force singularity of strength $\boldsymbol{f}$ applied to the point $\boldsymbol{x}_f$ is the Stokes equations,

$$\nabla \cdot \boldsymbol{u} = 0, \tag{A1}$$

$$\mu \nabla^2 \boldsymbol{u} = \nabla p - \boldsymbol{f}(\boldsymbol{x}_f) \delta(\boldsymbol{x} - \boldsymbol{x}_f), \tag{A2}$$

where $\mu$ is the fluid viscosity, and $\delta$ is the Dirac $\delta$ function. The solution of (A1) and (A2) (also known as the Stokeslet) reads

$$\boldsymbol{u}(\boldsymbol{x}) = \boldsymbol{S}(\boldsymbol{x}_f, \boldsymbol{x}) \boldsymbol{f}(\boldsymbol{x}_f), \tag{A3}$$

with

$$\boldsymbol{S}(\boldsymbol{x}_f, \boldsymbol{x}) = \frac{1}{8\pi\mu} \left( \frac{\mathbf{I}}{r} + \frac{(\boldsymbol{x}_f - \boldsymbol{x})(\boldsymbol{x}_f - \boldsymbol{x})}{r^3} \right), \tag{A4}$$

where $\mathbf{I}$ is the unit matrix and $r = \|\boldsymbol{x}_f - \boldsymbol{x}\|$. The tensor $\boldsymbol{S}(\boldsymbol{x}_f, \boldsymbol{x})$ is commonly indicated as the Oseen tensor.

The MFS [25] was already successfully employed in microfluidics, see, e.g., Refs. [38,39]. In brief, as shown in
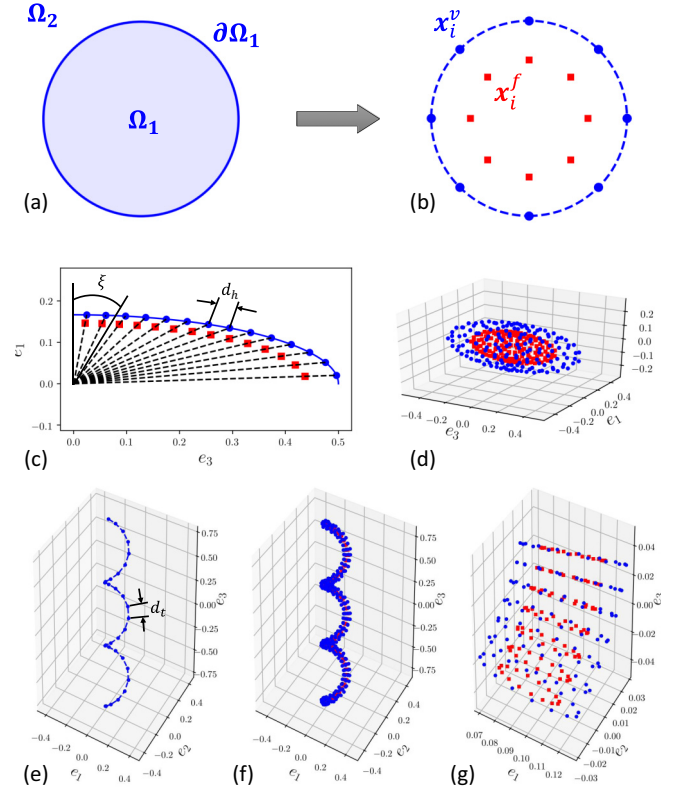


FIG. 4. Sketch of the method of fundamental solutions. (a) A solid body (domain $\Omega_1$) moves in a bulk fluid (domain $\Omega_2$). The solid blue line $\partial\Omega_1$ is the boundary of the solid body. Boundary points $\boldsymbol{x}_i^v$ (blue circles) are selected on $\partial\Omega_1$ whereas source points $\boldsymbol{x}_i^f$ (red squares) are placed inside the solid body. Panel (c) shows the discretization used for a quarter of an ellipse whereas the swimmer head is in panel (d). Panel (e) reports the tail centerline whereas panel (f) refers to the discretization of the swimmer tail. Each section of the tail is modeled as a circle where, again, red squares correspond to force sources and blue circles to the boundary. In panel (g) a short section of the swimmer tail is shown.

Figs. 4(a) and 4(b) for problems where the velocity is assigned on the boundary of a solid domain $\Omega_1$ and the velocity field needs to determined in the external domain $\Omega_2$, the key of the MFS is to find an approximation field $\boldsymbol{u}'$ that is defined in the domain $\Omega_1 \cup \Omega_2$ and that fulfills the boundary condition at the frontier of $\Omega_1$. The fluid velocity field $\boldsymbol{u}'$ is a smooth field that is defined in both domains $\Omega_1$ and $\Omega_2$. A set of $n$ boundary points $\boldsymbol{x}_i^v$ located at the boundary $\partial\Omega_1$ are selected. For each one of them, we know its corresponding velocity $\boldsymbol{u}(\boldsymbol{x}_i^v)$ from boundary conditions. A set of $n$ point forces is placed inside domain $\Omega_1$ close to the boundary points, the location of the point forces being indicated as $\boldsymbol{x}_i^f$. Hence, the velocity $\boldsymbol{u}(\boldsymbol{x}_i^v)$ can be expressed as

$$\begin{bmatrix} \boldsymbol{u}(\boldsymbol{x}_1^v) \\ \dots \\ \boldsymbol{u}(\boldsymbol{x}_n^v) \end{bmatrix} = \begin{bmatrix} \boldsymbol{S}(\boldsymbol{x}_1^f, \boldsymbol{x}_1^v) & \dots & \boldsymbol{S}(\boldsymbol{x}_n^f, \boldsymbol{x}_n^v) \\ & \ddots & \\ \boldsymbol{S}(\boldsymbol{x}_1^f, \boldsymbol{x}_1^v) & \dots & \boldsymbol{S}(\boldsymbol{x}_n^f, \boldsymbol{x}_n^v) \end{bmatrix} \begin{bmatrix} \boldsymbol{f}(\boldsymbol{x}_1^f) \\ \dots \\ \boldsymbol{f}(\boldsymbol{x}_n^f) \end{bmatrix}. \tag{A5}$$

This system has $3n$ unknowns and $3n$ equations. Once (A5) is solved for $\boldsymbol{f}$, the approximated velocity $\boldsymbol{u}'$ in a generic point

$x$ of the domain $\Omega_1 \cup \Omega_2$ can be calculated as

$$\boldsymbol{u}'(\boldsymbol{x}) = \sum_{i=1}^{n} \boldsymbol{S}(\boldsymbol{x}_i^f, \boldsymbol{x}) \boldsymbol{f}(\boldsymbol{x}_i^f). \tag{A6}$$

In the following, to simplify the notation, we will use the same symbol $\boldsymbol{u}$ for the approximated velocity and the true solutions of the Stokes problem.

### 2. The discretization of the microswimmer

A technical issue in MFS concerns the location $\boldsymbol{x}_i^f$ of the point sources. Our swimmer is composed by a spheroidal head and a helical tail. Concerning the head, we first placed the boundary point on a two-dimensional ellipse with semiaxes $r_{h1}$ and $r_{h2}$ lying on the $\boldsymbol{e}_3\boldsymbol{e}_1$ plane, approximately at the same distance $d_h$ [40,41], see Fig. 4(c). The ellipsoid is a body of revolution. Hence, we rotated each point around the major axis $\boldsymbol{e}_3$ of the ellipsoid obtaining a circle perpendicular to $\boldsymbol{e}_1$. This circle is divided into boundary points with equal distance $d_h$. In this paper, we select $d_h/r_{h1} \cong 0.047$ for a total of 1653 boundary points lying on the swimmer head and indicated as $\boldsymbol{x}_i^{vh}$.

For each boundary point $\boldsymbol{x}_i^{vh}$, a point force is located inside the ellipsoid on the lines that connect $\boldsymbol{x}_i^{vh}$ with the ellipsoid center $\boldsymbol{x}_c$. The distance $r_i^{fh}$ between $\boldsymbol{x}_c$ and $\boldsymbol{x}_i^{fh}$ is given by

$$r_i^{fh} = \delta_h r_i^{vh}, \quad \delta_h = 1 + \frac{2\epsilon_h \langle d_h \rangle}{(r_{h1} + r_{h2})}, \tag{A7}$$

where $r_i^{vh}$ is the distance between the ellipse center $\boldsymbol{x}_i^{vh}$, $\langle d_h \rangle$ is the average distance of the neighbor boundary points and $\epsilon_h$ is a control parameter. In this paper, we used $\epsilon_h = -1$. We also verified that results do not change for $\epsilon_h \in (-0.5, -1)$. Figure 4(d) shows an example of the ellipsoid after discretization.

Concerning the tail, we first defined its centerline in a reference system with the origin in the swimmer head center $\boldsymbol{x}_c$ as

$$\boldsymbol{r}_t(s) = [r_{t1}\cos(2\pi s), r_{t2}\sin(2\pi s), \lambda s - \delta_{bt}], \tag{A8}$$

where $s \in [-n/2, n/2]$ with $n$ as the number of periods of the tail, $\lambda$ is the pitch of the helix, $\delta_{bt}$ is the distance from $\boldsymbol{x}_c$ to the tail center, here set to $\delta_{bt} = r_{h1} + n\lambda/2 + r_{h1}/2$, and $r_{t1}$ and $r_{t2}$ are the radii of the elliptical cylinder on which the helix lies. We also performed a set of simulations analogous to the ones discussed in Fig. 3 but with $\delta_{bt} = r_{h1} + n\lambda/2 + r_{h1}/5$. Beside minor quantitative differences, the results fairly agree with the one discussed in the paper. We discretize $s$ into $m + 1$ values $s_i = -n/2 + in/m$, $i \in (0, m)$ as shown in Fig. 4(e). Then, for each of them, we put a circle of radius $\rho_t$ perpendicular to the centerline of the helix. This circle is divided into boundary points with equal distance $d_t$ The associated point forces are placed on the concentric circle that are perpendicular to the helix centerline as shown in Fig. 4(b). The radius of this concentric circle is $\rho_t - \epsilon_t d_t$ with $\epsilon_t = -1$. In this paper, we select $d_t = \sqrt{\lambda^2 + C_{elp}^2} n/m \cong 0.019$, where $C_{elp}$ indicates the perimeter of the ellipse with radii $r_{t1}$ and $r_{t2}$. The two ends of the helix are closed using semispheres. The generation method of the discretized semisphere is the same as one used for the ellipsoidal head of the microswimmer where, now, we used

$r_{h1} = r_{h2} = \rho_t$ whereas $d_t$ is the distance among the boundary points of the hemisphere.

Setting as the unit of length the larger axis of the ellipse, the circular helical tail microswimmers has the following geometrical parameters $r_{h1} = 1/2$, $r_{h2} = 1/6$, $r_{t1} = 0.1$, $r_{t2} = 0.1$, $\rho_t = 0.03$, $n = 3$, $\lambda = 2/3$. The number of point forces is 1653 for the head and 1534 for the tail. For the elliptical helical tail all the parameters are the same as for the circular tail swimmer with the exception of $r_{t1} = 0.3$. The number of point forces on elliptical helix tail is 2464.

### 3. Swimmer kinematics and boundary conditions

The microswimmer has seven DOFs, six DOFs represent the rigid motion of the head whereas the other the spinning of the tail. Without loss of generality, for the translational DOFs we selected the center $\boldsymbol{x}_c$ of the ellipsoid that constitutes the swimmer head, whereas for the orientational DOFs, we selected the angles $\phi$, $\theta$, and $\phi$ reported in Fig. 1. The associated translational and rotational velocities are here indicated as $\boldsymbol{U}$ and $\boldsymbol{\Omega}$. The tail rotates around the swimmer axis $\boldsymbol{p} \equiv \boldsymbol{e}_3$ at a spinning rate $\omega_t$ with respect to the head. The no-slip boundary condition is applied on the surfaces of the head and the tail of the microswimmer, hence, the fluid velocity at the swimmer boundary point is

$$\boldsymbol{u}(\boldsymbol{x}_i^{vh}) = \boldsymbol{U} + \boldsymbol{\Omega} \times \boldsymbol{r}_i^{vh} \tag{A9}$$

for the head boundary points $\boldsymbol{x}_i^{vh}$ and

$$\boldsymbol{u}_t(\boldsymbol{x}_i^{vt}) = \boldsymbol{U} + (\boldsymbol{\Omega} + \omega_t \boldsymbol{p}) \times \boldsymbol{r}_i^{vt}, \tag{A10}$$

for the tail boundary points $\boldsymbol{x}_i^{vt}$, where in both equations $\boldsymbol{r}_i$ indicates the relative position of the boundary point with respect to the center of the swimmer head $\boldsymbol{x}_c$. In our problem, the tail spin $\omega_t$ is given, and the other six DOFs are unknown. Thus, applying and (A10) into (A5), we get a system of $3n$ variables in $3n + 6$ unknowns. To complete this problem, we needed additional six equations that are the force- and torque-free conditions of the microswimmer,

$$\sum_{i=1}^{n_h} \boldsymbol{f}(\boldsymbol{x}_i^{fh}) + \sum_{i=1}^{n_t} \boldsymbol{f}(\boldsymbol{x}_i^{ft}) = 0, \tag{A11}$$

$$\sum_{i=1}^{n_h} \boldsymbol{r}_i^{fh} \times \boldsymbol{f}(\boldsymbol{x}_i^{fh}) + \sum_{i=1}^{n_t} \boldsymbol{r}_i^{ft} \times \boldsymbol{f}(\boldsymbol{x}_i^{ft}) = 0, \tag{A12}$$

obtaining a system of $3n + 6$ variables in $3n + 6$ unknowns.

The system was solved using the generalized minimal residual method [42] implemented in the portable, extensible toolkit for scientific computation (PETSc) [43,44]. The solution provides the rigid body translational $\boldsymbol{U}$ and rotational $\boldsymbol{\Omega}$ velocities of the microswimmer head and the $3n$ components of the point force from which using (A6) the entire velocity field can be built.

Once the swimmer head generalized velocity $(\boldsymbol{U}, \boldsymbol{\Omega})$ is obtained, the swimmer configuration is updated using the

following kinematic equations,

$$\frac{d\boldsymbol{x}_c}{dt} = \boldsymbol{U},$$ (A13)

$$\frac{d\boldsymbol{e}_i}{dt} = \boldsymbol{\Omega} \times \boldsymbol{e}_i, \quad i = 1\text{--}3,$$ (A14)

$$\frac{d\psi_t}{dt} = \omega_t.$$ (A15)

As commonly performed in microswimmer problems [10,45], in our code, we replaced (A14) with the quaternion formulation [46,47], to keep a higher numerical accuracy. Equations (A13)–(A15) were solved using a fourth order Runge-Kutta method [48] implemented in PETSc [44,49].

#### 4. The method of base flow

In principle, the swimming problem presented in the previous section needs to be solved at any time step of the Runge-Kutta integrator used to update the swimmer configuration. This will require a large amount of computational resources. Here we present an approach to largely speed up the simulation. This approach is based on the decomposition of the swimmer motion into two parts, an active part and a passive part. The idea of motion decomposition in the creep limit has a long history. For example, the motion of a particle in Stokes flow can be decoupled into the translation and the rotation parts [35,50]. Using this approach, Chwang and Wu [51] derived several exact solutions of the motion of a spheroid in a Stokes flow. Subramanian and Koch and Banerjee and Subramanian extended their work and discussed the orientation of a passive spheroid in the simple shear flow [52,53] and planar linear flow [54]. Analytical solutions of the microswimmer motion with arbitrary geometry in the five basis flows, however, is difficult. Hence, after decomposing the motion, we employed the numerical method of the fundamental solution (described in the previous section) to solve the Stokes problems.

More specifically, we decouple the swimmer kinematics as it follows: (i) the active part $(\boldsymbol{U}_a, \boldsymbol{\Omega}_a)$ corresponding to the microswimmer self-propelling in a bulk fluid at rest, and (ii) the passive part $(\boldsymbol{U}_p, \boldsymbol{\Omega}_p)$ corresponding to a passive microswimmer (i.e., no tail spinning, $\omega_t = 0$) in an external flow $\boldsymbol{u}_b$. In formulas,

$$\boldsymbol{U}(\boldsymbol{x}_c, \boldsymbol{\theta}_c, \psi_t) = \boldsymbol{U}_a(\boldsymbol{\theta}_c, \psi_t) + \boldsymbol{U}_p(\boldsymbol{x}_c, \boldsymbol{\theta}_c, \psi_t), \quad \text{(A16)}$$

$$\boldsymbol{\Omega}(\boldsymbol{x}_c, \boldsymbol{\theta}_c, \psi_t) = \boldsymbol{\Omega}_a(\boldsymbol{\theta}_c, \psi_t) + \boldsymbol{\Omega}_p(\boldsymbol{x}_c, \boldsymbol{\theta}_c, \psi_t). \quad \text{(A17)}$$

where we collectively indicated with $\boldsymbol{\theta}_c$ the three angles $\theta$, $\phi$, and $\psi$, see Fig. 1 defining the swimmer orientation.

*Active motion.* For the active part, we first numerically calculated the unit-spin motion $(\tilde{\boldsymbol{U}}_a, \tilde{\boldsymbol{\Omega}}_a)$ of a microswimmer swimming with $\omega_t = 1$ pointed toward the $\mathbf{X}_3$ direction with $(\theta = 0, \phi = 0, \psi = 0, \psi_t = 0)$. Thanks to the rotational symmetry of the ellipsoidal head, the last two rotational DOFs can be reduced to single DOF $\psi' = \psi + \psi_t$. Indeed, if we take a given conformation on the swimmer and we applied a rotation of the entire swimmer of an angle $\psi = \alpha$ and then a rotation of the tail with respect to the head of and angle $\psi_t = -\alpha$ the initial and the final conformations are the same. Therefore, we can easily transform the motion $(\boldsymbol{U}_a, \boldsymbol{\Omega}_a)$ of an active swimmer whose tail spins at a rate $\omega_t$ from the body coordinate frame $\mathbf{O}'\mathbf{e}_1\mathbf{e}_2\mathbf{e}_3$ to the global coordinate frame $\mathbf{OX}_1\mathbf{X}_2\mathbf{X}_3$,

$$\boldsymbol{U}_a(\boldsymbol{\theta}_c, \psi_t) = \omega_t \boldsymbol{R}(\boldsymbol{\theta}_c, \psi_t)\tilde{\boldsymbol{U}}_a,$$ (A18)

$$\boldsymbol{\Omega}_a(\boldsymbol{\theta}_c, \psi_t) = \omega_t \boldsymbol{R}(\boldsymbol{\theta}_c, \psi_t)\tilde{\boldsymbol{\Omega}}_a,$$ (A19)

where the rotation matrix $\boldsymbol{R}$ (that transforms the expression of a vector in the body reference frame into its expression in the global reference frame) is a function of $\theta$, $\phi$, and $\psi'$,

$$\boldsymbol{R} = \begin{bmatrix} \mathrm{C}\phi\mathrm{C}\psi'\mathrm{C}\theta - \mathrm{S}\phi\mathrm{S}\psi' & -\mathrm{C}\psi'\mathrm{S}\phi - \mathrm{C}\phi\mathrm{C}\theta\mathrm{S}\psi' & \mathrm{C}\phi\mathrm{S}\theta \\ \mathrm{C}\psi'\mathrm{C}\theta\mathrm{S}\phi + \mathrm{C}\phi\mathrm{S}\psi' & \mathrm{C}\phi\mathrm{C}\psi' - \mathrm{C}\theta\mathrm{S}\phi\mathrm{S}\psi' & \mathrm{S}\phi\mathrm{S}\theta \\ -\mathrm{C}\psi'\mathrm{S}\theta & \mathrm{S}\psi'\mathrm{S}\theta & \mathrm{C}\theta \end{bmatrix},$$ (A20)

where $\mathrm{S}\theta$ stands for $\sin(\theta)$ and $\mathrm{C}\theta$ stands for $\cos(\theta)$, and so on.

*Passive motion.* Now, we discuss the passive part $(\boldsymbol{U}_p, \boldsymbol{\Omega}_p)$ induced by the external flow $\boldsymbol{u}_b$. This is a quite classical problem that we briefly revise for completeness [35,50]. Taylor expansion allows to locally decompose the generic flow field $\boldsymbol{u}_b$ into three parts,

$$u_i^b(\boldsymbol{x}_c + \delta\boldsymbol{x}_c) = u_i^b(\boldsymbol{x}_c) + E_{ij}(\boldsymbol{x}_c)\delta x_j^c + S_{ij}(\boldsymbol{x}_c)\delta x_j^c, \quad \text{(A21)}$$

$$E_{ij}(\boldsymbol{x}_c) = \tfrac{1}{2}\big[u_{i,j}^b(\boldsymbol{x}_c) + u_{j,i}^b(\boldsymbol{x}_c)\big],$$ (A22)

$$S_{ij}(\boldsymbol{x}_c) = \tfrac{1}{2}\big[u_{i,j}^b(\boldsymbol{x}_c) - u_{j,i}^b(\boldsymbol{x}_c)\big],$$ (A23)

where $E_{ij}$ and $S_{ij}$ are the symmetric and asymmetric parts of the velocity gradient $u_{i,j} = \partial u_i/\partial x_j$. The first term on the right

hand side of (A21) gives a pure rigid body translation $\boldsymbol{U}_p^b(\boldsymbol{x}_c)$ of the microswimmer without rotation, see Fig. 5(b). Instead, the effect of the last term induced a pure rigid body rotation $\boldsymbol{\Omega}_p^S = \tfrac{1}{2}\nabla \times \boldsymbol{u}^b$ where the $\nabla \times \boldsymbol{u}^b$ is the bulk fluid vorticity, see Fig. 5(d). The contribution of the symmetric part of the gradient to the motion, Fig. 5(c), however, is more complex. $E_{ij}$ has nine components, but since it is symmetric, i.e., $E_{ij} = E_{ji}$, and the fluid is incompressible, i.e., $\mathrm{tr}(E_{ij}) = E_{ii} = 0$, only five of them are independent. Our approach is first to express the strain rate $E_{ij}$ in the body reference frame,

$$\tilde{E}_{ij} = R^T E_{ij} R,$$ (A24)

where $R$ is the rotation matrix (A20). Then, we decompose it in five basic modes due to the linearity of the Stokes equations
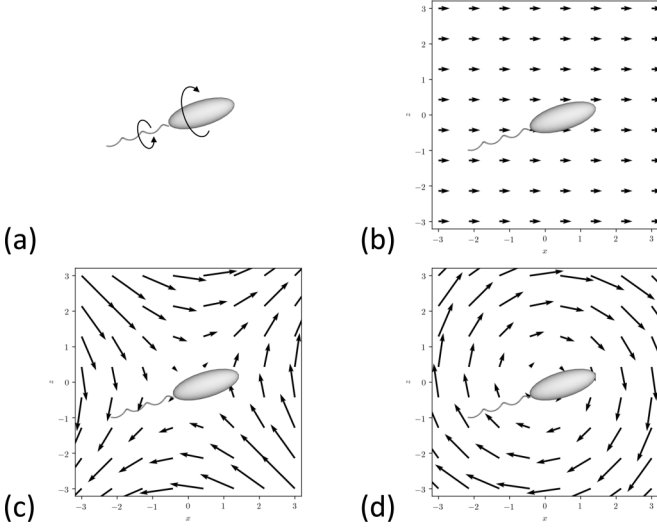
FIG. 5. Sketch of the kinetic decoupling of the microswimmer in an external flow. (a) Active microswimmer motion $(\tilde{U}_a, \tilde{\Omega}_a)$ in bulk fluid at rest. (b) Passive microswimmer translation $u_b$ in the external flow. (c) Passive microswimmer motion $(\tilde{U}^E, \tilde{\Omega}^E)$ in the symmetric (deviatoric) part of the external flow. (d) Passive microswimmer rotation $\Omega_p^S$ in the antisymmetric part of the external flow.

[50,51],

$$\tilde{E}_{ij} = \sum_{k=1}^{5} \tilde{\beta}_k \tilde{E}_{ij}^k. \tag{A25}$$

Indeed, any $\tilde{E}_{ij}^k$ can be expressed as

$$\tilde{E}_{ij} = \begin{bmatrix} \beta_1 & \beta_3 & \beta_4 \\ \beta_3 & -\beta_1 - \beta_2 & \beta_5 \\ \beta_4 & \beta_5 & \beta_2 \end{bmatrix}, \tag{A26}$$

by using the five components reported in Table I. Given this decomposition, we numerically solve the swimming kinematics $(\tilde{U}_k^E, \tilde{\Omega}_k^E)$ of the passive microswimmer for the five components and sum them with proper weights $\tilde{\beta}_k$,

$$\tilde{U}_p^E(x, \theta_c, \psi_t) = \sum_{k=1}^{5} \tilde{\beta}_k(x, \theta_c, \psi_t) \tilde{U}_k^E, \tag{A27}$$

$$\tilde{\Omega}_p^E(x, \theta_c, \psi_t) = \sum_{k=1}^{5} \tilde{\beta}_k(x, \theta_c, \psi_t) \tilde{\Omega}_k^E. \tag{A28}$$

Finally, we express $\tilde{U}_p^E$ and $\tilde{\Omega}_p^E$ in the global reference frame,

$$U_p^E(x, \theta_c, \psi_t) = R(\theta_c, \psi_t) \tilde{U}_k^E(x, \theta_c, \psi_t), \tag{A29}$$

$$\Omega_p^E(x, \theta_c, \psi_t) = R(\theta_c, \psi_t) \tilde{\Omega}_k^E(x, \theta_c, \psi_t). \tag{A30}$$

It is worth noting that the weights $\tilde{\beta}_k$, $k = 1 \cdots 5$ are functions of external flow $u_b$ and swimmer configuration $(\theta_c, \psi_t)$, and they do not vary with the geometric details of the microswimmer. Similar strategies for calculating the passive motion of the microswimmer can be found in Refs. [52,54].

TABLE I. Base flow associated with the decomposition of the symmetric component of the velocity gradient, see (A25).

| $k$ | Strain rate base $\tilde{E}_{ij}^k$ | Associated flow $\tilde{u}_i^{Ek}$ |
|---|---|---|
| 1 | $\begin{bmatrix} 1 & 0 & 0 \\ 0 & -1 & 0 \\ 0 & 0 & 0 \end{bmatrix}$ | $(x_1, -x_2, 0)$ |
| 2 | $\begin{bmatrix} 0 & 0 & 0 \\ 0 & -1 & 0 \\ 0 & 0 & 1 \end{bmatrix}$ | $(0, -x_2, x_3)$ |
| 3 | $\begin{bmatrix} 0 & 1 & 0 \\ 1 & 0 & 0 \\ 0 & 0 & 0 \end{bmatrix}$ | $(x_2, x_1, 0)$ |
| 4 | $\begin{bmatrix} 0 & 0 & 1 \\ 0 & 0 & 0 \\ 1 & 0 & 0 \end{bmatrix}$ | $(x_3, 0, x_1)$ |
| 5 | $\begin{bmatrix} 0 & 0 & 0 \\ 0 & 0 & 1 \\ 0 & 1 & 0 \end{bmatrix}$ | $(0, x_3, x_2)$ |

To summarize, the microswimmer generalized velocity in an external flow is obtained as

$$U = \omega_t R \tilde{U}_a + U_p^b + R \sum_{k=1}^{5} \tilde{\beta}_k \tilde{U}_k^E, \tag{A31}$$

$$\Omega = \omega_t R \tilde{\Omega}_a + \Omega_p^S + R \sum_{k=1}^{5} \tilde{\beta}_k \tilde{\Omega}_k^E. \tag{A32}$$

A sketch of the proposed decoupling is reported in Fig. 5. The main advantage of this method is that, for a given geometry of
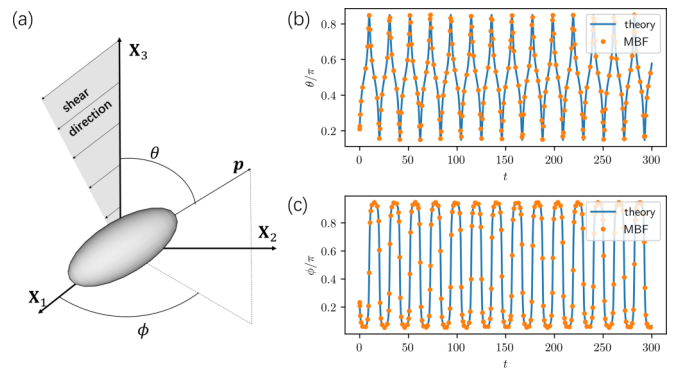


FIG. 6. Validation of the numerical method: Jeffery orbits. (a) Sketch of an ellipse orbit in a shear flow. The shear flow is on the $\mathbf{X}_1\mathbf{X}_3$ plane of the global coordinate frame $\mathbf{OX}_1\mathbf{X}_2\mathbf{X}_3$. The polar $\theta$ and azimuthal $\phi$ angles are used to describe the orientation of the body frame with respect to the global frame. The unit vector $\boldsymbol{p}$ denotes the orientation of the ellipsoid. (b) and (c) Time evolution of angles $\theta$ and $\phi$ for an ellipse with aspect ratio $r_{h1}/r_{h2} = 3$ moving in a shear flow. The initial orientation of the ellipse is $(\theta = 0.21\pi, \phi = 0.23\pi)$. Orange points represent our numerical solution whereas the analytical solution [35] are reported as blue lines.

the microswimmer, regardless the tail spin rate $\omega_t$, only six simulations are necessary; one for getting $(\tilde{U}_a, \tilde{\boldsymbol{\Omega}}_a)$ and five for $(\tilde{\boldsymbol{u}}_k^E, \tilde{\boldsymbol{\Omega}}_k^E)$, $k = 1 \cdots 5$. Thus, one can obtain these quantities accurately previously, and then solve the microswimmer kinematics (A13)–(A15).

For the microswimmer motion in the shear flow $\boldsymbol{u}_b = (X_3, 0, 0)$, we have

$$E_{ij} = \frac{1}{2} \begin{bmatrix} 0 & 0 & 1 \\ 0 & 0 & 0 \\ 1 & 0 & 0 \end{bmatrix}, \qquad (A33)$$

that, using (A24) and (A25), gives

$$\tilde{\beta}_1 = C\psi'(S\phi S\psi' - C\phi C\psi' C\theta)S\theta, \qquad (A34)$$

$$\tilde{\beta}_2 = C\phi C\theta S\theta, \qquad (A35)$$

$$\tilde{\beta}_3 = \tfrac{1}{4}[2C(2\psi')S\phi S\theta + C\phi S(2\psi')S(2\theta)], \qquad (A36)$$

$$\tilde{\beta}_4 = \tfrac{1}{2}[C\phi C\psi' C(2\theta) - C\theta S\phi S\psi'], \qquad (A37)$$

$$\tilde{\beta}_5 = \tfrac{1}{2}[-C\psi' C\theta S\phi - C\phi C(2\theta)S\psi']. \qquad (A38)$$

To test our approach, we reproduced the Jeffery orbit [55] for a $r_{h1}/r_{h2} = 3$ ellipse in a shear flow, see Fig 6.

[1] H. C. Berg, *E. coli in Motion* (Springer, New York, 2008).

[2] C. Qian, C. C. Wong, S. Swarup, and K.-H. Chiam, Bacterial tethering analysis reveals a "run-reverse-turn" mechanism for pseudomonas species motility, Appl. Environ. Microbiol. **79**, 4734 (2013).

[3] P. Sartori, E. Chiarello, G. Jayaswal, M. Pierno, G. Mistura, P. Brun, A. Tiribocchi, and E. Orlandini, Wall accumulation of bacteria with different motility patterns, Phys. Rev. E **97**, 022610 (2018).

[4] L. Zhang, K. E. Peyer, and B. J. Nelson, Artificial bacterial flagella for micromanipulation, Lab on a Chip **10**, 2203 (2010).

[5] R. Mhanna, F. Qiu, L. Zhang, Y. Ding, K. Sugihara, M. Zenobi-Wong, and B. J. Nelson, Artificial bacterial flagella for remote-controlled targeted single-cell drug delivery, Small **10**, 1953 (2014).

[6] E. Lauga and T. R. Powers, The hydrodynamics of swimming microorganisms, Rep. Prog. Phys. **72**, 096601 (2009).

[7] J. Elgeti, R. G. Winkler, and G. Gompper, Physics of microswimmers-single particle motion and collective behavior: A review, Rep. Prog. Phys. **78**, 056601 (2015).

[8] E. Lauga, W. R. DiLuzio, G. M. Whitesides, and H. A. Stone, Swimming in circles: Motion of bacteria near solid boundaries, Biophys. J. **90**, 400 (2006).

[9] G. Guccione, D. Pimponi, P. Gualtieri, and M. Chinappi, Diffusivity of e. coli-like microswimmers in confined geometries: The role of the tumbling rate, Phys. Rev. E **96**, 042603 (2017).

[10] H. Shum, E. A. Gaffney, and D. J. Smith, Modelling bacterial behavior close to a no-slip plane boundary: The influence of bacterial geometry, Proc. R. Soc., Ser. A **466**, 1725 (2010).

[11] R. Di Leonardo, D. Dell-Arciprete, L. Angelani, and V. Iebba, Swimming with an Image, Phys. Rev. Lett. **106**, 038101 (2011).

[12] D. Pimponi, M. Chinappi, P. Gualtieri, and C. M. Casciola, Hydrodynamics of flagellated microswimmers near free-slip interfaces, J. Fluid Mech. **789**, 514 (2016).

[13] J. Hu, A. Wysocki, R. G. Winkler, and G. Gompper, Physical sensing of surface properties by microswimmers–directing bacterial motion via wall slip, Sci. Rep. **5**, 9586 (2015).

[14] S. Bianchi, F. Saglimbeni, G. Frangipane, D. Dell'Arciprete, and R. D. Leonardo, 3d dynamics of bacteria wall entrapment at a water–air interface, Soft Matter **15**, 3397 (2019).

[15] H. C. Fu, T. R. Powers, and R. Stocker, Bacterial rheotaxis, Proc. Natl. Acad. Sci. USA **109**, 4780 (2012).

[16] Marcos, H. C. Fu, T. R. Powers, and R. Stocker, Separation of Microscale Chiral Objects by Shear Flow, Phys. Rev. Lett. **102**, 158103 (2009).

[17] R. Rusconi, J. S. Guasto, and R. Stocker, Bacterial transport suppressed by fluid shear, Nat. Phys. **10**, 212 (2014).

[18] P. Kanehl and T. Ishikawa, Fluid mechanics of swimming bacteria with multiple flagella, Phys. Rev. E **89**, 042704 (2014).

[19] E. E. Riley, D. Das, and E. Lauga, Swimming of peritrichous bacteria is enabled by an elastohydrodynamic instability, Sci. Rep. **8**, 10728 (2018).

[20] J. Einarsson, B. M. Mihiretie, A. Laas, S. Ankardal, J. R. Angilella, D. Hanstorp, and B. Mehlig, Tumbling of asymmetric microrods in a microchannel flow, Phys. Fluids **28**, 013302 (2016).

[21] J. Einarsson, Angular dynamics of small particles in fluids, Ph.D. thesis, University of Gothenburg, 2015.

[22] I. Thorp and J. Lister, Motion of a non-axisymmetric particle in viscous shear flow, J. Fluid Mech. **872**, 532 (2019).

[23] H. C. Berg and L. Turner, Torque generated by the flagellar motor of escherichia coli, Biophys. J. **65**, 2201 (1993).

[24] J. Xing, F. Bai, R. Berry, and G. Oster, Torque–speed relationship of the bacterial flagellar motor, Proc. Natl. Acad. Sci. USA **103**, 1260 (2006).

[25] D. L. Young, S. J. Jane, C. M. Fan, K. Murugesan, and C. C. Tsai, The method of fundamental solutions for 2d and 3d stokes problems, J. Comput. Phys. **211**, 1 (2006).

[26] See Supplemental Material at http://link.aps.org/supplemental/10.1103/PhysRevE.103.023109 for movies showing these trajectories and for a figure representing the dependence of the final stable trajectory on initial swimmer orientation **p** are reported together with a diagram representing the domains in the orientation space that led to II₁, II₂, II₃ trajectories.

[27] H. C. Berg, Motile behavior of bacteria, Physics Today **53**(1), 24 (2000).

[28] B. Liu, K. S. Breuer, and T. R. Powers, Propulsion by a helical flagellum in a capillary tube, Phys. Fluids **26**, 011701 (2014).

[29] C. Rorai, M. Zaitsev, and S. Karabasov, On the limitations of some popular numerical models of flagellated microswimmers: Importance of long-range forces and flagellum waveform, R. Soc. Open Sci. **6**, 180745 (2019).

[30] R. Cortez, L. Fauci, and A. Medovikov, The method of regularized stokeslets in three dimensions: analysis, validation, and application to helical swimming, Phys. Fluids **17**, 031504 (2005).

[31] B. Zhang, Y. Ding, and X. Xu, Active suspensions of bacteria and passive objects: A model for the near field pair dynamics, arXiv:2002.04693.

[32] E. Klaseboer, Q. Sun, and D. Y. C. Chan, Non-singular boundary integral methods for fluid mechanics applications, J. Fluid Mech. **696**, 468 (2012).

[33] G. P. Muldowney and J. J. L. Higdon, A spectral boundary element approach to three-dimensional stokes flow, J. Fluid Mech. **298**, 167 (1995).

[34] A. J. T. M. Mathijssen, N. Figueroa-Morales, G. Junot, É. Clément, A. Lindner, and A. Zöttl, Oscillatory surface rheotaxis of swimming e. coli bacteria, Nat. Commun. **10**, 1 (2019).

[35] S. Kim and S. J. Karrila, *Microhydrodynamics: Principles and Selected Applications* (Courier, New York, 1991).

[36] A. Najafi and R. Golestanian, Simple swimmer at low reynolds number: Three linked spheres, Phys. Rev. E **69**, 062901 (2004).

[37] A. Daddi-Moussa-Ider, M. Lisicki, and A. J. T. M. Mathijssen, Tuning the upstream swimming of microrobots by shape and cargo size, Phys. Rev. Appl. **14**, 024071 (2020).

[38] Y. Aboelkassem and A. E. Staples, Stokeslets-meshfree computations and theory for flow in a collapsible microchannel, Theor. Comput. Fluid Dyn. **27**, 681 (2013).

[39] D. A. Lockerby and B. Collyer, Fundamental solutions to moment equations for the simulation of microscale gas flows, J. Fluid Mech. **806**, 413 (2016).

[40] Considering one-quarter of an ellipse, the arc length is a monotone increasing function of the eccentric angle $\xi$ that has no explicit expression. Therefore, we first fit this function using a quadratic polynomial then determine a set of $\xi_i$, $i \in (1, n_h)$ that keeps the distance between two adjacent points approximately equal. Finally we calculate the location of the points on the $\mathbf{e}_3\mathbf{e}_1$ plane, see Ref. [41].

[41] A. Jones, How to divide an ellipse to equal segments? [https://stackoverflow.com/questions/20197974/how-to-divide-an-ellipse-to-equal-segments (2013)] [Online; accessed 6-August-2020].

[42] Y. Saad and M. H. Schultz, Gmres: A generalized minimal residual algorithm for solving nonsymmetric linear systems, SIAM J. Sci. Stat. Comput. 7, 856 (1986).

[43] S. Balay, W. D. Gropp, L. C. McInnes, and B. F. Smith, Efficient management of parallelism in object-oriented numerical software libraries, *Modern Software Tools for Scientific Computing* (Springer, Berlin, 1997), pp. 163–202.

[44] S. Balay, S. Abhyankar, M. F. Adams, J. Brown, P. Brune, K. Buschelman, L. Dalcin, A. Dener, V. Eijkhout, W. D. Gropp, D. Karpeyev, D. Kaushik, M. G. Knepley, D. A. May, L. C. McInnes, R. T. Mills, T. Munson, K. Rupp, P. Sanan, B. F. Smith, S. Zampini, H. Zhang, and H. Zhang, PETSc Web page, https://www.mcs.anl.gov/petsc (2019).

[45] D. Pimponi, M. Chinappi, and P. Gualtieri, Flagellated microswimmers: Hydrodynamics in thin liquid films, Eur. Phys. J. E **41**, 1 (2018).

[46] B. Graf, Quaternions and dynamics, arXiv:0811.2889.

[47] J. Diebel, Representing attitude: Euler angles, unit quaternions, and rotation vectors, Matrix **58**, 1 (2006).

[48] P. Bogacki and L. F. Shampine, An efficient runge-kutta (4, 5) pair, Comput. Math. Appl. **32**, 15 (1996).

[49] S. Abhyankar, J. Brown, E. M. Constantinescu, D. Ghosh, B. F. Smith, and H. Zhang, Petsc/ts: A modern scalable ode/dae solver library, arXiv:1806.01437.

[50] J. Happel and H. Brenner, *Low Reynolds Number Hydrodynamics: With Special Applications to Particulate Media* (Springer, Berlin, 2012), Vol. 1.

[51] A. T. Chwang and T. Wu, Hydromechanics of low-reynolds-number flow. part 2. singularity method for stokes flows, J. Fluid Mech. **67**, 787 (1975).

[52] G. Subramanian and D. L. Koch, Inertial effects on the orientation of nearly spherical particles in simple shear flow, J. Fluid Mech. **557**, 257 (2006).

[53] M. R. Banerjee and G. Subramanian, An anisotropic particle in a simple shear flow: An instance of chaotic scattering, J. Fluid Mech. **913**, A2 (2021).

[54] N. K. Marath and G. Subramanian, The inertial orientation dynamics of anisotropic particles in planar linear flows, J. Fluid Mech. **844**, 357 (2018).

[55] G. B. Jeffery, The motion of ellipsoidal particles immersed in a viscous fluid, Proc. R. Soc. London, Ser. A **102**, 161 (1922).